# The Role of Side Chains and Hydration on Mixed Charge Transport in n -Type Polymer Films

Jokūbas Surgailis, Lucas Flagg, Lee J Richter, Victor Druet, Sophie Griggs, Xiaocui Wu, Stefania Moro, David Ohayon, Christina J Kousseff, Adam Marks, et al.

ADVANCED MATERIALS
www.advmat.de

# The Role of Side Chains and Hydration on Mixed Charge Transport in *n*-Type Polymer Films

*Jokūbas Surgailis, Lucas Q. Flagg, Lee J. Richter, Victor Druet, Sophie Griggs, Xiaocui Wu, Stefania Moro, David Ohayon, Christina J. Kousseff, Adam Marks, Iuliana P. Maria, Hu Chen, Maximilian Moser, Giovanni Costantini, Iain McCulloch, and Sahika Inal**

**Introducing ethylene glycol (EG) side chains to a conjugated polymer backbone is a well-established synthetic strategy for designing organic mixed ion-electron conductors (OMIECs). However, the impact that film swelling has on mixed conduction properties has yet to be scoped, particularly for electron-transporting (*n*-type) OMIECs. Here, the authors investigate the effect of the length of branched EG chains on mixed charge transport of *n*-type OMIECs based on a naphthalene-1,4,5,8-tetracarboxylic-diimide-bithiophene backbone. Atomic force microscopy (AFM), grazing-incidence wide-angle X-ray scattering (GIWAXS), and scanning tunneling microscopy (STM) are used to establish the similarities between the common-backbone films in dry conditions. Electrochemical quartz crystal microbalance with dissipation monitoring (EQCM-D) and in situ GIWAXS measurements reveal stark changes in film swelling properties and microstructure during electrochemical doping, depending on the side chain length. It is found that even in the loss of the crystallite content upon contact with the aqueous electrolyte, the films can effectively transport charges and that it is rather the high water content that harms the electronic interconnectivity within the OMIEC films. These results highlight the importance of controlling water uptake in the films to impede charge transport in *n*-type electrochemical devices.**

## 1. Introduction

Organic mixed ion-electron conductors (OMIECs) typically refer to conjugated polymer films capable of conducting ionic and electronic charges.[1,2] Not only do OMIEC films conduct both types of carriers, but also facilitate their coupling, so that the presence of one type of charge influences the transport of the other, establishing a transduction mechanism between the electronic and ionic signals. The organic electrochemical transistor (OECT) has emerged as a prominent device utilizing the coupled charge transport properties of OMIEC films. In an OECT, small ionic signals at the gate electrode are transduced into readable electronic currents at the OMIEC channel as a result of mixed conduction. The key difference between the OECT and a field-effect transistor (FET) is that under the application of a gate-source voltage ($V_{GS}$), the OECT channel undergoes charging within its

J. Surgailis, V. Druet, D. Ohayon, S. Inal
King Abdullah University of Science and Technology (KAUST)
Biological and Environmental Science and Engineering Division
Organic Bioelectronics Lab
Thuwal 23955–6900, Saudi Arabia
E-mail: sahika.inal@kaust.edu.sa

L. Q. Flagg, L. J. Richter
National Institute of Standards and Technology (NIST)
Materials Science and Engineering Division
Gaithersburg, MD 20899, USA

S. Griggs, C. J. Kousseff, I. P. Maria, M. Moser, I. McCulloch
University of Oxford
Department of Chemistry
Chemistry Research Laboratory
Oxford OX1 3TA, UK

X. Wu, S. Moro, G. Costantini
Department of Chemistry
University of Warwick
Coventry CV4 7AL, UK

S. Moro, G. Costantini
School of Chemistry
University of Birmingham
Birmingham B15 2TT, UK

A. Marks
Department of Materials Science and Engineering
Stanford University
450 Serra Mall, Stanford, CA 94305, USA

H. Chen, I. McCulloch
KAUST
KAUST Solar Center
Physical Science and Engineering Division
Thuwal 23955–6900, Saudi Arabia



**DOI: 10.1002/adma.202313121**

entire volume (referred to as bulk ion (de)doping), which is reflected in a capacitance scaling linearly with film volume, that is, volumetric capacitance ($C^*$). The large $C^*$, when combined with high electronic charge mobility of the channel material ($\mu$), results in high transistor transconductance ($g_m$) values expressed as follows.[3]

$$g_m = \frac{\partial I_{DS}}{\partial V_{GS}} = \frac{Wd}{L}\mu C^* \left(V_{GS} - V_T\right) \quad (1)$$

where $I_{DS}$ is the channel current, $W$, $d$, and $L$ are the channel width, thickness, and length, respectively, and $V_T$ is the threshold voltage. The high $g_m$ and the low-voltage operation, inherent to electrolyte gating, render OECTs attractive for numerous applications (e.g., digital circuits,[4] biochemical sensors,[5,6] wearable electronics,[7,8] neuromorphic computing[9,10]), especially considering the biocompatibility and solution processability of OMIECs.

For blended polymeric systems, the conduction of two types of charges happens in separate phases of the film, such as in poly(3,4-ethylenedioxythiophene):poly(styrene sulfonate) (PEDOT:PSS), where electron/hole transport occurs in the PEDOT-rich phase, while ion transport takes place in the percolating PSS network.[11,12] For homogeneous, single-component systems, these separate phases can be considered analogous to the amorphous and crystalline regions. It is commonly accepted that a crystalline structure promotes electronic charge transport, while a water-swollen amorphous network allows for hydrated ion migration in the film.[13] However, it is unclear how these phases generate a final morphology with the transport pathways and which region governs or limits the transport. Moreover, while $\mu$ and $C^*$ are normally considered intrinsic to a material, both are non-trivially dependent on the morphology of the film at the electrochemical doping conditions. This dependency stems from the fact that, while an OMIEC may have its intrinsic material properties $\mu_{dry}$ and $C^*_{dry}$ in a dry state, adding water and ions to the system (through passive exposure or active biasing) alters the system equilibrium and essentially creates a new material, with new intrinsic properties $\mu_{wet/doped}$ and $C^*_{wet/doped}$. The way these properties vary depends on the interactions between the OMIEC and the electrolyte and can be difficult to predict, necessitating various types of in situ measurements to establish a property-bias dependency curve. Designing polymer structures that can maximize these two parameters and generate a morphology ideal for the transport of both charges has, therefore, been challenging, particularly for electron-transporting (*n*-type) OMIECs,[14–17] also due to the oxygen reduction reactions that the *n*-type building blocks undergo at OECT operation voltages.

The first *n*-type OMIEC and OECT were demonstrated by Giovannitti et al., who synthesized a donor–acceptor type copolymer based on the electron-deficient 2,6-dibromonaphthalene-1,4,5,8-tetracarboxylic diimide (NDI) unit and the electron-rich bithiophene (T2),[18] namely p(gNDI-gT2). This polymer is reminiscent of p(NDI2OD-T2) (or N2200), which is renowned for its use in organic FETs.[19] The p(NDI2OD-T2) backbone could be utilized as a mixed-conduction material when the branched alkyl side chains on the NDI unit were replaced with linear ethylene glycol (EG) ones. Non-polar alkyl chains are commonly tethered to the backbone to ease processability by making the polymers soluble in organic solvents but play no role in the OFET operation. On the contrary, in addition to enabling polymer solubility in common organic solvents, polar EG side chains facilitate the insertion of aqueous electrolyte ions in the film by increasing their miscibility. The glycolated microenvironment takes up the electrolyte (passive swelling), solvates ions, and allows their transport within the film volume, leading to the volumetric nature of charge coupling and, ultimately, enabling OECT operation. However, follow-up work has shown evidence of the adverse effect that a high glycol side chain density in the polymer structure can have on electronic charge transport.[20] A trade-off between $C^*$ and $\mu$ was demonstrated by characterizing the electrochemical and OECT performances of NDI-T2-based random block copolymers bearing EG and alkyl side chains in different ratios.[20] Further studies using this backbone found a correlation between the volume changes that the films undergo during operation and the device performance. By designing polymers that swell less (by increasing the distance between the backbone and the EG units), the charge transport ability improved at the expense of ion uptake capability.[21] Another study modified the NDI moiety into a core-extended NDTI unit that planarized the backbone and improved film packing, which, in turn, reduced swelling and enhanced the OECT performance.[22] Jeong et al. investigated the effects of varying the length and symmetry of branched EG side chains on the performance of an NDI-T-based polymer.[23] Passive film swelling was directly proportional to the glycol density per repeat unit, varying from 328% to 22% for the film with the highest glycol content to the one with the lowest, respectively. The work showed that reducing film swelling increased $C^*$, suggesting an enhanced electrochemical doping efficiency of the film that takes up less water. Reducing the EG content and introducing asymmetry also changed the chain packing orientation from face-on to edge-on, improving electron transport.

The effects of side chain composition and film swelling on mixed conduction properties have also been observed with *n*-type backbones other than NDIs. Chen et al. compared two lactam-based, rigid, and planar *n*-type polymers, one bearing an EG and an alkyl side chain (PgNaN) and one with only EG side chains (PgNgN).[24] The balanced hydrophilic/hydrophobic character of PgNaN was thought to hinder reduce over-swelling, with performance over an order of magnitude higher than the PgNgN variant. Marks et al. expanded on the fused lactam *n*-type study by varying the alkyl side chain length from 2 to 16 carbons (lowest and highest hydrophobic fraction, respectively), hence tuning the ratio of hydrophilicity/hydrophobicity.[25] Both $\mu$ and $C^*$ had a non-monotonic dependence on the hydrophilic/hydrophobic character of the polymers, where variants containing 10 and 8 carbons displayed the highest values for both. This study demonstrates the non-trivial dependence of the OMIEC mixed conductance properties on the film's hydrophilicity/hydrophobicity.

Although these studies suggest a link between lower hydration and performance, they often compare polymers that exhibit distinct dry microstructures. This diversity in initial characteristics restricts the ability to attribute all observed properties solely to hydration. Nevertheless, it is clear that while swelling "enables" OECT operation, it does not enhance device performance indefinitely; therefore, simply increasing the hydrophilic content in an OMIEC is not a viable design strategy. Active swelling, on the other hand, which is normally a sign of ion and water uptake

upon biasing, often leads to the decline of $g_m$. The device $g_m$ (the primary OECT figure of merit) often peaks at a certain polymer swelling, beyond which it declines.[20,26,27] The non-monotonic dependence of $g_m$ with respect to film swelling is the first hint towards the complexity of device performance versus swelling. Some studies have shown that $\mu$ and $C^*$ may also show a non-monotonic dependency on swelling, where $\mu$ requires a certain level of swelling before it reaches its optimal value, but $C^*$ appears to plateau and roll over when the film swells too much.[28,29] High active swelling has been associated with increased disorder of the film structure and eventual disintegration of the electronic film interconnectivity.[12,26,30] However, some studies have shown that mixed conduction can and does happen in both amorphous and crystalline regions, with electronic charges being carried across disordered regions by so-called "tie chains" and ionic charges intercalating within ordered domains of the film.[30–32] While the malleability of the OMIEC film structure may be dubious for electronic charge transport, it is a prerequisite for the transport of solvated ions and, ultimately, charge coupling. Another important figure of merit affected by swelling is $V_T$. While higher swelling has mostly been associated with easier OECT switch-on due to more readily injected ionic charges, it has been shown that $V_T$ has a non-monotonic dependence on swelling, too, where beyond a certain limit of hydrophilicity, switching the device on becomes harder.[21] Considering all these findings and, still, the absence of clear guidelines for *n*-type OMIEC design, understanding the full scope of the effects swelling on the electrochemical and device operation of OMIECs, including the underlying mechanisms, is crucial for advancing OECT-based technologies.

In this study, we investigate the electrochemical properties of four *n*-type polymers that contain an identical NDI-T2-based backbone with branched EG side chains of varying lengths. The main interest lies in how the varying side chains affect film formation upon casting and its interactions with aqueous electrolytes associated with charge injection and retention during electrochemical operation. We first characterize the physical film properties in the dry state using atomic force microscopy (AFM), grazing-incidence wide-angle X-ray scattering (GIWAXS), and scanning tunneling microscopy (STM). We then inspect how the films behave upon exposure to the electrolyte solution using UV–vis spectroscopy and under biasing using quartz crystal microbalance with dissipation monitoring (QCM-D) and in situ GIWAXS. The results confirm the greater affinity of the longer side chain variants to water and the varying degrees of electrolyte insertion into the polymer films. We show that increasing side chain length leads to an exponential increase in water uptake with seemingly little increase in the number of cations compensating the electrons. Additionally, we characterize micrometer-scale OECTs bearing the polymers in the channel, followed by independent measurements of $C^*$ and calculation of $\mu$, which are the material mixed conduction figures of merit. We find that longer hydrophilic side chains lead to diminished device performance before any tangible benefits can be gleaned. Shortening the side chain length appears to maximize not only the $\mu$ but, surprisingly, also the $C^*$. The latter observation contradicts the existing notion that the ion-electron coupling capability of polymer films is improved by increased polymer hydrophilicity. Interestingly, we also find that even with disrupted crystallinity, the devices remain operable and stable, suggesting charge transport can still take place efficiently within the amorphous film domains.

## 2. Results

### 2.1. Film Morphology and Microstructure in Dry State

The chemical structures of the polymers, p(1gNDI-T2), p(2gNDI-T2), p(3gNDI-T2), and p(4gNDI-T2), are shown in **Figure 1a**. The variants will henceforth be referred to as 1g, 2g, 3g, and 4g, in accordance with the previously established naming convention.[22] Before proceeding with operando characterization, we first wanted to establish if there were any characteristic differences between the four variants in their dry state. We first probed the absorbance signals of each variant dissolved in chloroform (Figure S1, Supporting Information) and in a dry film state (Figure 1b). A slight trend can be observed in the solution spectra between the branched side chain variants, wherein the intramolecular charge transfer (ICT) absorbance feature, located around 600 nm, appears to decrease in intensity with respect to the normalized $\pi$–$\pi^*$ feature at 400 nm when increasing side chain length. The lower intensity of the ICT peak suggests a lower charge-transfer rate from the donor to the acceptor with increasing side chain length. All thin film spectra show a red shift compared to the solution state. The resultant dry films display a red shift of 30 nm, going from 1g to 4g, with minimal differences observed between 2g and 4g. The apparent redshift might be a result of altered vibronic transition ratios, where the shortest side chain variant exhibits an increased 0–2 transition (≈650 nm), whereas the longer side chain variant displays an increased 0-0 transition (≈800 nm), with the 0–1 transition placed in between the two (≈700 nm). These vibronic peak transitions from 0-0 to 0–2 have been associated with a transition between form I and form II packing, where the former exhibiting aligned stacking ($NDI_n$ on $NDI_{n-1}$) and the latter exhibiting mixed stacking ($NDI_n$ on $T2_{n-1}$).[33]

The surface morphology of all films is similar, with a root mean square (RMS) roughness lower than 2 nm (Figure 1c). All four films present some fibrillar structure with visible aggregation breaking out of the film plane, which has been observed for similar OMIECs.[34,35] 4g displays a somewhat inhomogeneous morphology compared to the rest of the films. Investigating the phase scans (Figure S2, Supporting Information), we observe that 3g and 4g display two distinguishable phase regions with about 2 to 3 degrees of difference in the phase angle. On the other hand, 1g and 2g present a more homogeneously distributed phase contrast. Contact angle measurements suggest a trend of almost monotonically increasing hydrophilicity with longer side chain lengths, with the most significant difference observed between 1g and 4g (Table S1, Supporting Information).

GIWAXS measurements suggest that all four films have similar crystal texture with a notable out-of-plane $\pi$-stacking feature near 1.7 $Å^{-1}$, an in-plane lamellar spacing near 0.3 $Å^{-1}$, and a *c*-axis feature (periodicity along the backbone) near 0.5 $Å^{-1}$ consistent with a face-on orientation, similar to other NDI polymers[23,35] (Figure 1d). The lamellar spacing is shorter than what would be expected if the side chains were fully extended and the polymers were laterally packed by mere juxtaposition, suggesting some form of side chain compacting, whether by

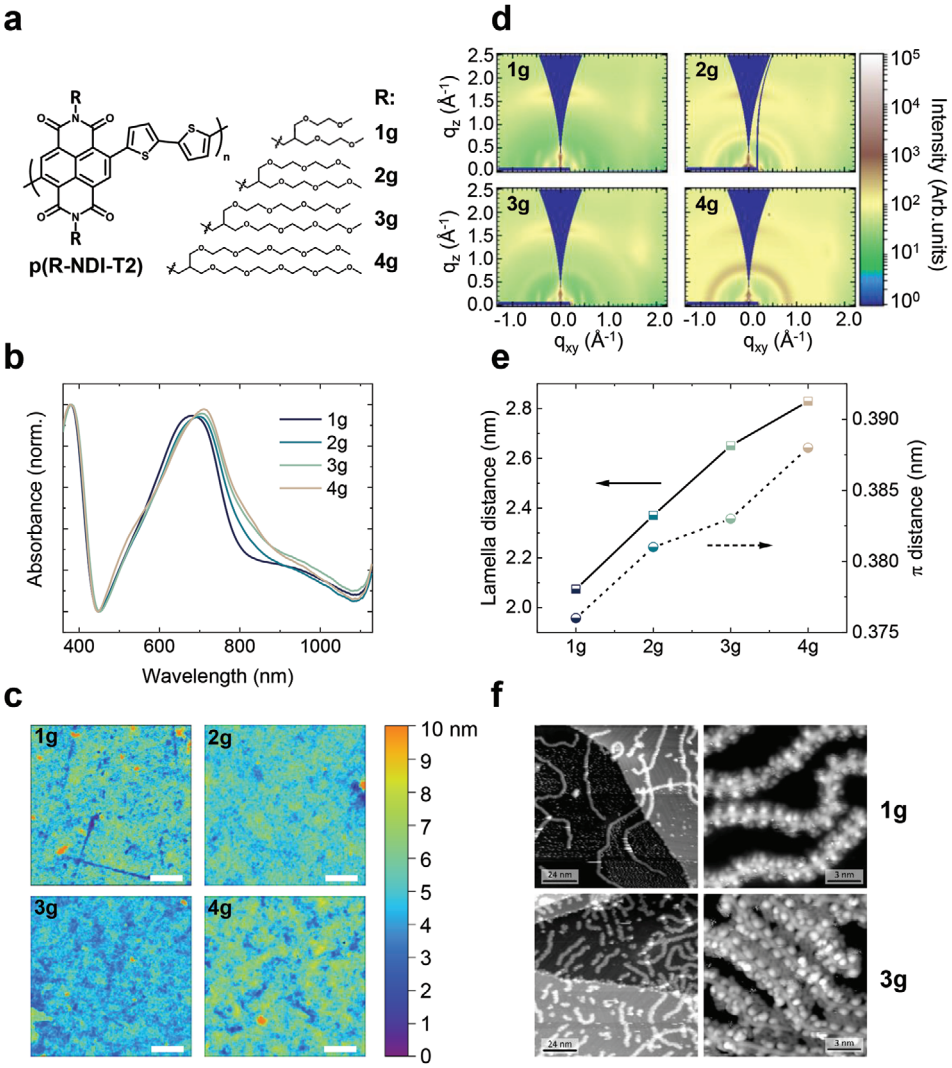


**Figure 1.** a) Chemical structure of the p(R-NDI-T2) polymer and its side chain variants. b) Dry UV–vis spectra of the four polymer films. c) AFM topography images. Images are of 5 × 5 µm film areas, and the scale bar corresponds to 1 µm. d) GIWAXS 2D images of dry films (the rings around 0.8 $Å^{-1}$ are artifacts from silicone grease). e) The corresponding lattice *d*-spacing values were calculated from the locations of the (100) peak and (010) peak (Table S2, Supporting Information) and are plotted as a function of side chain length. The reported GIWAXS distance values have an estimated standard error of ± 0.01 nm. f) Large-scale (left) and high-resolution (right) STM images of low surface coverage areas of 1g (top row) and 3g (bottom row). The imaging conditions are: $V = 677$ mV, $I = 78$ pA (top left image); $V = 677$ mV, $I = 58$ pA (top right image); $V = 484$ mV, $I = 78$ pA (bottom left image); $V = 176$ mV, $I = 90$ pA (bottom right image).

interdigitation, overlap, or self-interaction. It was recently shown that, unlike their alkyl counterparts, EG side chains tend to adopt twisted/coiled configurations, leading to higher variability in how the backbones pack.[36] As the side chain gets longer, the lamellar spacing expands (Figure 1e, and Table S2, Supporting Information). The expansion in the lamellar spacing when going from 1g to 4g is accompanied by a slight (3%) expansion in the $\pi$-stacking direction.

One caveat is the differences in the mass-average molecular mass ($M_w$) of the four variants. As measured by gel permeation chromatography (GPC), 1g appears to have a significantly greater $M_w$ of 95.3 kDa, compared to the fairly intermediate $M_w$ of 2g and 3g (49.9 and 40.7 kDa, respectively), with 4g having the lowest $M_w$ (22.0 kDa). Considering that GPC may overestimate the $M_w$ of OMIECs due to aggregation of glycolated materials in solution,[37] we inspected the molecular lengths of 1g and 3g using STM. This was achieved by depositing the polymers onto an atomically clean and flat single crystalline Au(111) surface through electrospray deposition under vacuum conditions, followed by in situ ultrahigh vacuum STM imaging of their microstructure.[36,38–41] From the large-scale STM images shown in the left column of Figure 1f, the length of individual polymers was measured, and the average length and mass were estimated by a statistical analysis on a large number of chains. The analysis of the STM data revealed considerably lower masses when compared with the GPC data, giving an estimated $M_w$ for 1g and 3g of 31 and 18 kDa, respectively. The relative trend of the polymer masses, however, remained unchanged, with 1g appearing

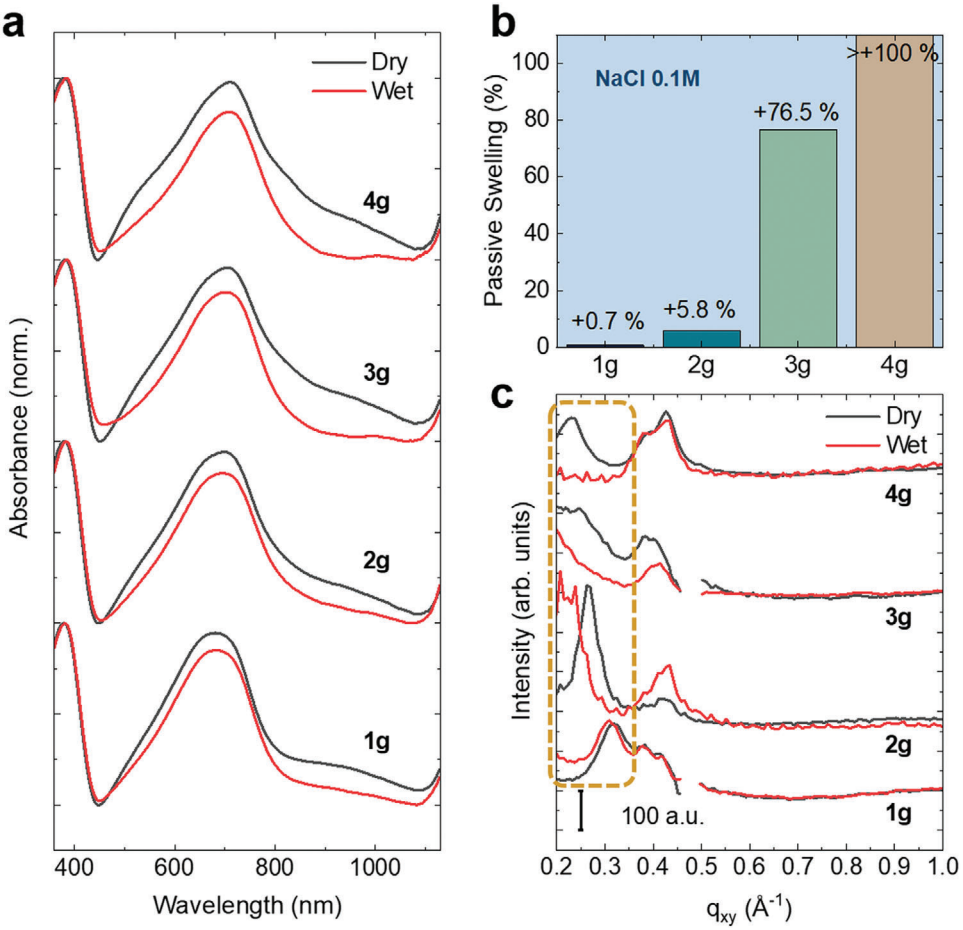


**Figure 2.** a) UV–vis spectra of the polymer films in dry state (black) and wet state in 0.1 mol $L^{-1}$ NaCl (red). b) Passive film swelling in 0.1 mol $L^{-1}$ NaCl calculated from QCM-D measurements. c) In situ GIWAXS (in-plane) taken in both dry states (black) and exposed to 0.1 mol $L^{-1}$ NaCl (red). Relevant features are highlighted with the orange box. The features around 0.4 Å$^{-1}$ are artifacts due to the Kapton window and not film crystals.

to be about double the length of 3g. A recent report showed that varying the $M_w$ of an NDI-based OMIEC by up to a full order of magnitude did not lead to any obvious changes in either $\mu$ or $C^*$.[42] Regardless, it is worth keeping in mind that since 1g has a higher $M_w$ than the others in the series, if we observe a transport performance unique for this polymer, this may be a consequence of its longer overall chain length. On the other hand, we can confidently attribute the wet behavior differences between 2g and 3g to their differing interactions with electrolytes, as these polymers have similar morphologies in the dry state and molecular weight.

Close-up STM images (right column in Figure 1f) grant access to the precise 2D microstructure of the polymers at the sub-monomer scale. It is possible to discern the polymer backbones, characterized by continuous line-shaped features, which are flanked on both sides by bright dots, indicating the starting points of the polymer side chains. The distance between two consecutive bright dots was measured to be 1.4 ± 0.1 nm for both 1g and 3g, which is in good agreement with the theoretically expected one (1.46 nm, see Figure S3, Supporting Information). The STM images also show that the EG side chains adopt a curly conformation,[36] giving a first indication of why the lamellar spacing values observed by GIWAXS are shorter than expected. At high polymer coverage, the distance between neighboring backbones in closely packed regions can be measured directly from the STM images (Figure S4, Supporting Information), showing an expansion of the 2D lamellar spacing from 2.2 nm for 1g to 2.6 nm for 3g. These values are consistent with the corresponding 3D lamellar spacing values obtained from the GIWAXS measurements (Table S2, Supporting Information). Recalling the previously observed red-shift from 1g to 4g in dry UV–vis (Figure 1b), we do not observe the associated changes in (00l) scattering, which were described for P(NDI2OD-T2) upon the transition from form I to form II.[43] These findings suggest a similar crystalline structure for all polymers, while for 1g, the molecular weight might be affecting the overall structure of the film, possibly giving rise to a blue-shifted ICT peak maximum (Figure 1b).

### 2.2. Swollen Film Morphology and Microstructure

**Figure** 2a shows how the film UV–vis spectra change when the films are immersed in an aqueous NaCl solution. All four variants exhibit a downward shift in intensity in the 500 to 1100 nm

range, compared to the $\pi$–$\pi^*$ transition. The absorbance of the longer side chain variants (3g and 4g) in the 900 to 1000 nm range is fully bleached, while the other two variants (1g and 2g) retain their features. These results indicate greater structural rearrangements for the longer side chain variants induced by the electrolyte. The observed changes in the spectrum when transitioning from the dry to wet state are likely due to the higher affinity of the longer side chains to water. We inspected film hydration directly using quartz crystal microbalance with dissipation monitoring (QCM-D), which tracks the changes in vibration frequency and decay of a quartz crystal sensor upon its exposure to an electrolyte, enabling the mass and the viscoelastic property modeling of polymer films coated on the sensor. We quantified how much each polymer film swells in 0.1 mol $L^{-1}$ aqueous NaCl solution by exposing the dry films to the electrolyte and summarized these results (referred to as "passive swelling") in Figure 2b. Increasing side chain length exacerbates film swelling, where the shortest side chain variant, 1g, exhibits virtually no passive swelling (0.7%), while the longest side chain variant, 4g, swells hugely to the point that it is difficult to quantify the mass change accurately (> 110%), most likely due to film hydrogelation. It is also very interesting to observe the abrupt change in swelling when going from 2g (~6%) to 3g (~77%), that are, polymers with very similar molecular weight, and the only difference in their structure being one oligoether unit in the side chain.

While dry film characterization did not reveal major differences between the microstructure of the polymers, the swollen film GIWAXS images reveal changes in crystalline packing upon the spontaneous uptake of the electrolyte (Figure 2c). While the 1g and 2g variants show some lamellar expansion in the wet state (~2% and ~19%, respectively), the longer side chain variants show a complete disappearance of the crystal signals around 0.2 to 0.3 $Å^{-1}$. The absence of crystal signals in 3g and 4g can be interpreted as "melting". We hypothesize that the polymer crystals in the films bearing the long-branched side chains (3g and 4g) become disordered by the ingress of aqueous electrolyte molecules. These side chains have a greater affinity to water than the intermolecular interactions keeping polymer chains packed in crystallites. Importantly, there is no delamination of the films, suggesting the films transitioned into an amorphous state. It is worth noting that the transition from a persistent to a disappearing crystal signal occurs between 2g and 3g, two polymers with nearly identical molecular weights and dry microstructures but distinctly different responses to electrolyte exposure, driven by variations in their side chain lengths. Additionally, despite 1g having a higher molecular weight than the other variants in the series, it exhibits the least swelling due to its shorter side chain length. The crystallite expansion trends, as obtained from GIWAXS, are summarized in Table S3, Supporting Information.

### 2.3. Films under Electrochemical Biasing

The cyclic voltammetry (CV) curves in **Figure** 3a show that all variants undergo reversible electrochemical doping in the *n*-type regime and are fairly stable under subsequent cycles. The onset reduction potentials in ambient conditions are roughly similar for all polymers (approximately −0.28 V) with no clear correlation to side chain length. The largest CV current density is that of the shortest side chain variant, 1g, indicating the largest extent of electrochemical charging over the same potential range. Furthermore, 1g displays the most defined redox peaks of all the polymers, the most pronounced being the secondary peak at around −0.7 V. From the remaining variants, only 4g shows a distinguishable secondary reduction peak, but to a significantly lesser degree. Performing the measurement in a deoxygenated environment reveals "flatter" CVs with a more equal distribution of cathodic and anodic currents as the Faradaic oxygen reduction reaction (ORR) currents are eliminated (Figure 3a, and Figure S5, Supporting Information).[44] The deoxygenated CV curves display a trend in onset potentials, which increase from −0.25 V (4g) to −0.38 V (1g) with decreasing side chain length (Figure S5, Supporting Information). Interestingly, the extent to which the CVs were shifted by the presence of $O_2$ seems to increase with increasing side chain length, where 4g shows the most significant difference between the two conditions, while the shift in 1g appeared to be minimal. The apparent decrease in ORR currents with decreasing side chain length suggests that there is a correlation between the water affinity and the ORR rate of the OMIEC film.

To understand how much the films expand or contract during their reduction and oxidation, we used electrochemical QCM-D (EQCM-D). We applied a series of doping and de-doping potentials once the films reached equilibrium swelling in the electrolyte, which caused the films to swell and de-swell, and estimated the extent of these mass changes ("active swelling"). Figure 3b shows that with each increasing doping voltage (> −0.2 V vs Ag/AgCl), the films take up additional mass and release this mass partially when a de-doping voltage (0 V vs Ag/AgCl) is applied. We do not display the swelling profile of 4g, as the film exhibited swelling beyond what could be accurately quantified using QCM-D. From the active swelling results, it becomes clear that increasing side chain length leads to exponentially more swelling at corresponding doping potentials.

In situ GIWAXS allows us to see the changes induced in the crystalline domains during doping-induced electrolyte injection into the films. In Figure S6, Supporting Information, we show the heatmaps of the in-plane scattering signal evolution of 1g and 2g, noting that these are the only two films exhibiting in situ diffraction as the other films no longer show any scattering peaks in response to electrochemical cycling. While some modulation in the scattering can be observed (see traced line), these changes are marginal (5% for 1g and 7% for 2g when doped at −0.9 V vs Ag/AgCl) compared to the swelling rates obtained from EQCM-D (Table S4, Supporting Information). The discrepancy suggests that the vast majority of the electrolyte permeates the amorphous domains, interacting minimally with the crystalline ones. There is no significant decrease in $\pi$-packing distance (Table S4, Supporting Information), which has been observed in *p*-type OMIECs upon electrochemical doping,[45] meaning the backbone charging with ions has no beneficial impact on crystalline packing, if not dissolving them completely, as we revealed for 3g and 4g.

Further understanding can be obtained from the active swelling process by considering the measured mass uptake as a sum of ion and water mass. The ions enter the film with a surrounding solvation shell and possibly additional stray water, depending on electrolyte concentration, film morphology, and its

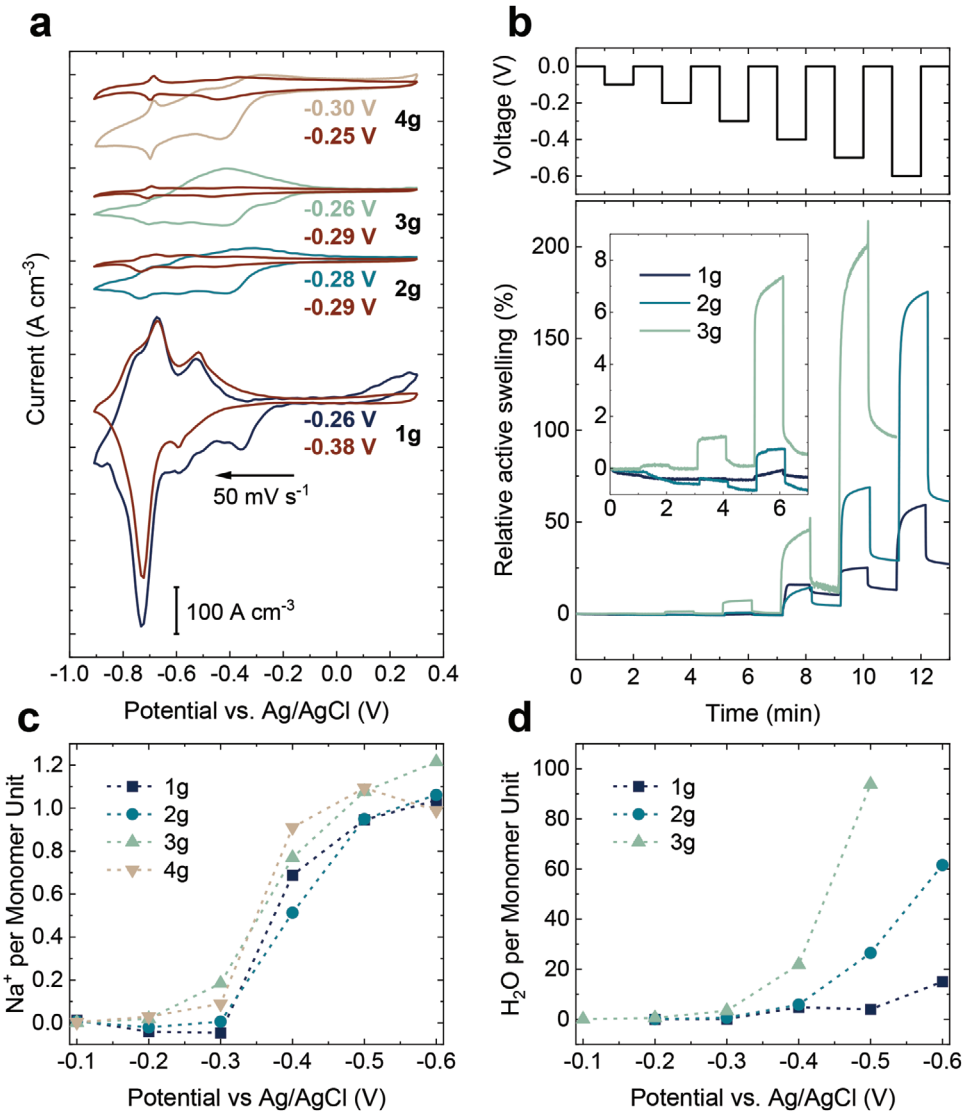


**Figure 3.** a) Cyclic voltammetry curves of the films recorded at a 50 mV $s^{-1}$ scan rate in ambient and deoxygenated electrolyte, along with electrochemical onset potentials reported in each case. b) Relative active swelling in response to incrementally increased doping potentials, obtained using EQCM-D. Inset shows a blown-up scale of the early stages of swelling. Decomposition of mass uptake into c) $Na^+$ and d) $H_2O$ amount per polymer repeat unit, using the current data recorded simultaneously.

water affinity.[26,28,46] The deconvolution of mass is done using Faraday's law of electrolysis, that is, the electronic charge injected into the films is used to calculate the number of cations entering the film, assuming that each cation couples with one electron. Knowing the mass of injected cations from the measured current allows us to assign the remaining mass to water and to obtain the number of $Na^+$ and $H_2O$ molecules per monomer unit injected into the films during electrochemical doping. Note that we do not consider any contribution from anions in these calculations. Figure 3c shows that the four variants accommodate a similar total amount of $Na^+$ ions injected into the films until −0.6 V, and the $Na^+$ amount taken up increases with voltage. However, among the three variants, a clear trend is seen where the longer the side chain is, the more water enters the film (Figure 3d). The amount of water that enters the film increases with the doping voltage but appears to have little impact on ion uptake ability. At a doping potential of −0.5 V, the four variants take up around 0.9 to 1.1 $Na^+$ ions per monomer unit. However, the water amount ranges from 4 to 26 to 94 $H_2O$ molecules per monomer unit, for 1g, 2g, and 3g, respectively, (4g not shown as the total mass could not be quantified due to over-swelling). Evidently, the longer side chain variants do not exhibit enhanced ion-electron coupling; instead, the long side chains appear to cause only an increased water uptake and overall film swelling.

### 2.4. Materials Mixed Conduction Figure of Merits

We next fabricated OECTs with these polymers as thin films in microscale channels, gated using an Ag/AgCl reference electrode

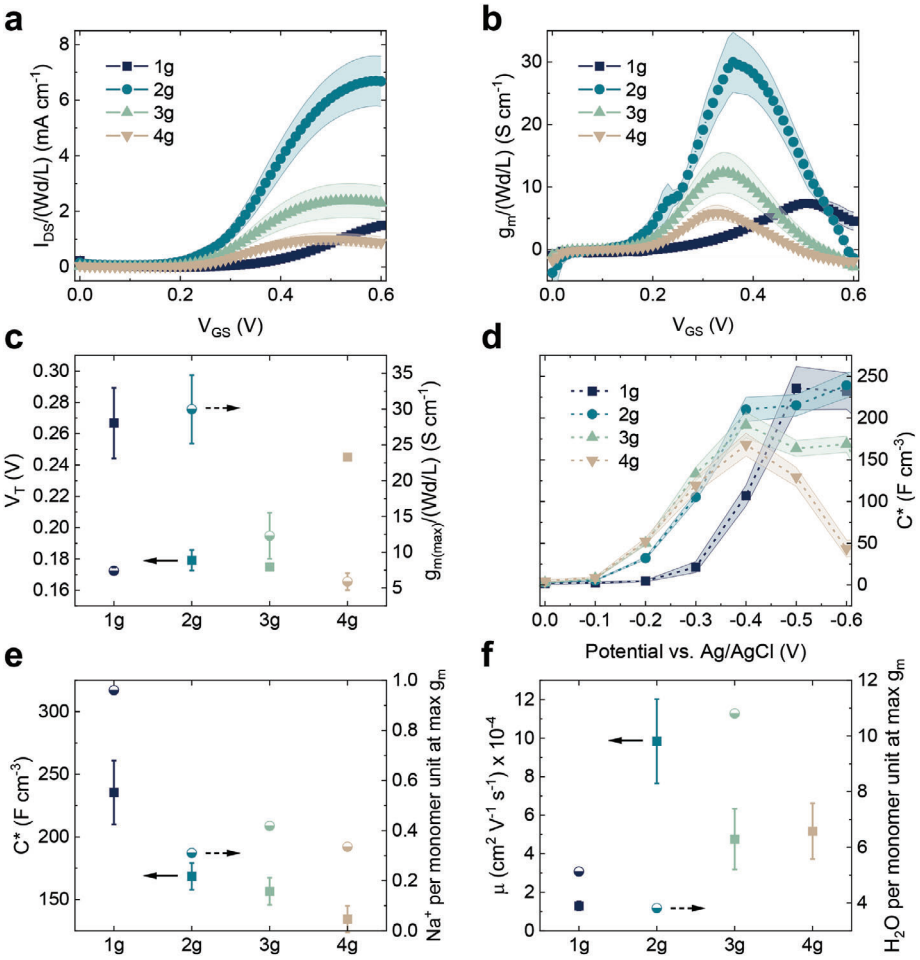


**Figure 4.** Geometry normalized a) transfer and b) transconductance curves of all four variants obtained from OECT characterization. Characterization was done on interdigitated OECT channels, comprising equivalent width and length of 2500 and 5 µm, respectively. c) Threshold voltage and peak transconductance value trends. d) Volumetric capacitance, obtained using electrochemical impedance spectroscopy performed using electrodes of varying sizes, as a function of doping voltages. e) $C^*$ at $g_{m(max)}$ and corresponding ion content taken up by the film. f) Electronic mobility values, calculated from $g_{m(max)}$, and the water content taken up by the film.

through an aqueous 0.1 mol L$^{-1}$ NaCl solution. **Figure** 4a,b show that the side chain length significantly affects the transfer and $g_m$ characteristics of the *n*-type OECTs. Increasing the side chain length leads to progressively lower ON currents and smaller maximum $g_m$ values, with the exception of 1g, which exhibits the second to lowest values of $I_{DS}$ and $g_m$. The higher molecular weight of this film appears to offer no advantage for mixed transport and may somewhat counteract the positive effect of a short side chain length. With the polymer having higher hydrophilicity, an earlier channel conductivity modulation is possible but not guaranteed.[21] The $V_T$ shifts to lower voltages when going from 1g to 3g (Figure 4c) but increases again from 3g to 4g. While a delayed turn-on is expected for a device consisting of a more hydrophobic channel due to the lack of pre-diffused ions, the similar onset of 4g with the 1g remains to be explained. On the other hand, peak transconductance ($g_{m(max)}$) is observed at increasingly lower gate voltages with increasing side chain length, with 1g and 4g peaking at 0.51 and 0.33 V, respectively (**Table** 1).

To better understand the origins of the side chain-modulated device performance, we separated the mixed conduction materials figure of merit, $\mu C^*$, into its components: $\mu$ and $C^*$. We estimated the film capacitance using electrochemical impedance spectroscopy (EIS) measurements performed at various doping potentials using films with differing geometries. We investigated $C^*$ as a function of doping biases to probe the different levels of channel doping induced by the gate. Figure 4d shows that the side chain length dictates the film capacitive response onset, where the most hydrophilic polymer of the series, 4g, shows the earliest response and 1g shows the latest. This result suggests that higher hydrophilicity allows the film to be charged at a lower potential, which overall correlates with the OECT $V_T$. We see a clear trend of decreasing peak $C^*$ with increasing side chain length. Specifically, 1g and 2g reach maximum values at 235.8 and 239.2 F cm$^{-3}$, respectively, while 3g and 4g peak at 191.6 and 168.2 F cm$^{-3}$, respectively (Figure 4e). We note that the largest drop in $C^*$ (around 40 F cm$^{-3}$) occurs when transitioning from 2g and 3g, despite these two polymers having almost identical dry film features such as $M_w$, underscoring the significant impact of swelling on the $C^*$ values. Note that the $C^*$ values cited here are the maximum values as observed from EIS. Table 1 includes $C^*$

**Table 1.** OECT characterization summary for all four polymer variants ($n = 4$). The channel width ($W$) and length ($L$) were 2500 and 5 µm, respectively.

| Metric | Unit | 1g | 2g | 3g | 4g |
|---|---|---|---|---|---|
| $V_T$ [a] | mV | 267 ± 23 | 179 ± 7 | 175 ± 2 | 245 ± 2 |
| On/off ratio [b] | | $1.2 \times 10^3$ | $0.1 \times 10^3$ | $0.3 \times 10^3$ | $0.1 \times 10^3$ |
| $V_{GS}$ ($g_{m(max)}$) [c] | V | 0.51 | 0.36 | 0.34 | 0.33 |
| $g_{m(max)}/(Wd/L)$ | mS cm$^{-1}$ | 7.4 ± 0.5 | 30.0 ± 4.8 | 12.3 ± 3.2 | 5.9 ± 1.2 |
| $\mu C^*$ [d] | mF cm$^{-1}$ V$^{-1}$ s$^{-1}$ | 30.8 ± 2.0 | 166.5 ± 26.6 | 76.0 ± 26.6 | 73.7 ± 14.9 |
| $C^*$ [e] | F cm$^{-3}$ | 235.5 ± 25.5 | 168.4 ± 10.6 | 156.5 ± 10.8 | 134.3 ± 10.5 |
| $\mu$ [f] | cm$^2$ V$^{-1}$ s$^{-1}$ (× $10^{-4}$) | 1.29 ± 0.22 | 9.83 ± 2.19 | 4.76 ± 1.58 | 5.17 ± 1.45 |
| Response time [g] | ms | 368.4 ± 33.6 | 99.2 ± 0.1 | 107.5 ± 30.5 | 97.2 ± 0.5 |

[a] Obtained from the slope of the $\sqrt{I_{DS}}$ versus $V_{GS}$ curve; [b] Obtained by calculating $I_{DS(max)}/I_{DS(min)}$; [c] The $V_{GS}$ that maximizes $g_m$; [d] Calculated by dividing the $g_{m(max)}$ with channel geometry $Wd/L$ and overdrive voltage ($V_{GS}$ - $V_T$); [e] Obtained using EIS measurements performed on MEAs with varying electrode sizes; values shown are corresponding to $C^*$ at $V_{GS}$ ($g_{m(max)}$); [f] Calculated by dividing $\mu C^*$ by $C^*$; [g] Obtained from the first 10 pulses of the stability measurements for each polymer shown in Figure S7, Supporting Information by calculating the time it took for the channel current to reach 95% of its final value.

values corresponding to the peak $g_m$ values, which occur at different potentials than the peak $C^*$ values. The decrease in $C^*$ with side chain length affirms that increasing hydrophilicity is not de facto beneficial for ion uptake, a conclusion QCM-D results also revealed. In fact, the increasing side chain length might be correlated to the decrease in the electrochemically active film fraction, causing a reduction in observed $C^*$ as shown here and in our previous study comparing the side chain-free BBL to a glycol bearing NDI-T2.[35] However, although the decrease in $C^*$ appears to be gradual and correlated to the increasing side chain length, it is impossible to completely discount the potential impact of $M_w$ on $C^*$, which is lowest for 4g and highest for 1g.

Finally, we calculated $\mu$ values from $g_{m(max)}$ using the corresponding $C^*$ values at the same biasing conditions (see Experimental Section in Supporting Information, Table 1). Figure 4f shows that among 2g, 3g, and 4g, the shortest side chain facilitated the highest mobility. Surprisingly, despite its low susceptibility to swelling, 1g exhibited the lowest $\mu$ (possibly due to its high $M_w$, making it an outlier in the trend). Among the variants, the 2g displayed the highest value of $\mu$ at $9.8 \times 10^{-4}$ cm$^2$ V$^{-1}$ s$^{-1}$, which along with its high $C^*$, led to the highest OECT performance among the variants. The remaining 3g and 4g variants show moderate but similar $\mu$ values despite exhibiting significant water uptake, as well as crystallite dissolution in the electrolyte. We also report the device response times in Table 1. While 1g showed the slowest response time at around 370 ms, correlated with its high $C^*$, the remaining three variants exhibited a response time of around 100 ms, showing no correlation with side chain length.

## 3. Discussion

We investigated the effect of side chain length and polymer overall hydrophilicity on the electrochemical operation and OECT performance of four NDI-T2-based polymers. Starting with the dry films, we observed slight side chain length-related differences in film morphology and phase, apparent as higher surface inhomogeneity manifesting in the more hydrophilic variants. Dry film GIWAXS, on the other hand, revealed minimal differences in crystalline packing, with a small expansion in the $\pi$ and lamella directions, the latter being also confirmed by STM images of 2D polymer films. The changes in packing can be explained by the increased volume occupied by the longer side chains, which tend to adopt a curled-up conformation, as shown by STM. Hence, the dry film crystalline domains seem to be mostly unaltered by changes in the side chain length.

The side chain length clearly affects how much the film swells when immersed in the electrolyte. The increased affinity to water by the longer side chains became obvious in the passive swelling trends obtained from QCM-D. The full extent of this spontaneous electrolyte insertion was revealed in the scattering signals, which disappeared for the swollen 3g and 4g, suggesting a complete disorder of the crystalline domains.

Despite the stark differences discussed so far between the two shorter and the two longer side chain variants, CV measurements in Figure 3a showed a comparable *n*-type operation across the series, with the exception of 1g, which exhibited considerably higher currents which is in agreement with the higher $C^*$ obtained for this film. For films with similar chain lengths, increasing the side chain length only inflated the water content in the film, with little apparent impact on ion uptake ability. The unencumbered swelling, along with the fact that increasing side chain length decreases the fraction of electrochemically active film volume, explains the decreasing $C^*$ from 2g to 3g. Once again, it remains difficult to assign the decrease in $C^*$ when transitioning from 1b to the other variants to effects of side chain length only, as the differences in $M_w$ somewhat obscure these results. However, keeping in mind that charge formation on NDI-based polymers is localized on the acceptor moiety and does not extend beyond the monomer unit, one could claim that $M_w$ may not have a significant role on $C^*$, but this has yet to be explored and established.

The high water content in the film is definitely not beneficial for charge transport; in fact, it disrupts the crystalline structure for the long EG length variants. The low charge transport mobility with the longer side chain variants lowers the device current and transconductance. Nevertheless, it is noteworthy that 3g and 4g still displayed moderate OECT operation despite apparently retaining none of their crystallinity upon exposure to the electrolyte, as shown by GIWAXS. Retained OECT operation

despite high film swelling has been previously observed in p(g3T2), where the film was shown to swell nearly 250%, while still displaying comparable OECT metrics and electronic mobility of up to 0.9 $cm^2\ V^{-1}\ s^{-1}$.[47] Szumska et al. demonstrated that excessive electrolyte uptake of NDI-T2-based polymers led to film instability and degradation during electrochemical cycling.[27] We, on the other hand, show that excess swelling has no impact on operational stability (Figure S7, Supporting Information). The film that swells to a level that disrupts scattering peaks demonstrates virtually full retention of its channel current after 3 h of cycling (over 500 on–off cycles).

The persistent operation of the crystallite-deprived 3g and 4g suggests that the amorphous regions play an important role in charge transport, even in the absence of a crystalline phase within the film. Conversely, the short side chains and long backbones of 1g may have led to improved device performance, but a lack of interconnectivity across the amorphous regions may be the reason for low mobilities, leading to an inability to utilize the potential benefits of the higher crystallite packing in the wet state. Note also that reduced electronic mobility with increased film crystallinity has been observed in P3MEEMT, where the annealed film could not sustain electronic transport upon hydration, as the crystalline region interconnectivity was disrupted by swelling.[30] Electronic mobility is highest in 2g, moderate in 3g and 4g, and severely diminished in 1g. The observed behavior in $\mu$ suggests that i) crystallite retention is non-essential for electronic transport, as evidenced by 3g and 4g, and ii) crystallite presence alone does not guarantee efficient electronic transport, which also relies on the transport capability of the amorphous regions.

While the results presented in this study provide valuable insights into the potential adverse effects of film hydrophilicity and swelling on *n*-type mixed conduction properties, it is important to note that the scope of this research has been limited to NDI-T2 derivatives. Future investigations exploring the impacts of side chain length and film hydration on *n*-type mixed conduction and OECT properties would greatly benefit from examining newer and higher performance *n*-type backbones synthesized in recent years, such as the ones based on fused bithiophene imide dimer,[48] isoindigo,[49] and fused lactam.[25] Leveraging these high-performance *n*-type OMIECs to advance fundamental research is sure to yield deeper insights into *n*-type mixed conduction mechanisms.

## 4. Conclusion

In this study, we explored the ramifications of uncontrolled water uptake on *n*-type OECT operation, by varying the oligoether length in the side chains of the NDI-T2-based backbone. While water uptake is inevitable during electrochemical and OECT operation, unconstrained water permeation harms electronic conduction. While intrinsically semi-crystalline, past a sufficient side chain length, the OMIEC films became disordered upon contact with the aqueous electrolyte. However, the dissolution of the crystalline domains did not lead to a breakdown of electronic mobility. The films that swell have lower OECT performance but can be reliably operated in the OECTs despite the loss of crystalline structure within the bulk. An important finding was that, in addition to severely diminishing electronic mobility, increasing side chain length did not improve the volumetric capacitance, suggesting that ion-electron coupling does not benefit from increased OMIEC hydrophilicity. While the full extent of the effects of water content, molecular weight, and volumetric capacitance is yet to be elucidated and warrants a dedicated study on its own, we expect that the findings given here will be pertinent to OECT materials that fall in the category of hydrophilic OMIECs.

## Supporting Information

Supporting Information is available from the Wiley Online Library or from the author.

## Acknowledgements

X.W. acknowledges co-funding from the European Union's Horizon 2020 research and innovation Marie Skłodowska-Curie Actions, under grant agreement no. 945380. S.M. acknowledges funding through an EU Chancellor's Scholarship by the University of Warwick. This publication is based upon work supported by King Abdullah University of Science and Technology (KAUST) Research Funding (KRF) under Award No. ORA-2021-CRG10-4650. G.C. and S.M. acknowledge support from a UK - Saudi Challenge Fund grant from the British Council's Going Global Partnerships programme. This research used beamline 11-BM (CMS) of the National Synchrotron Light Source, a U.S. Department of Energy (DOE) Office of Science User Facility operated for the DOE Office of Science by Brookhaven National Laboratory under contract no. DE-SC0012704. J.S. thanks Yizhou Zhong and Wentao Shan for providing devices for OECT characterization.

Open access publishing facilitated by King Abdullah University of Science and Technology, as part of the Wiley – King Abdullah University of Science and Technology (KAUST) agreement.

## Conflict of Interest

The authors declare no conflict of interest.

## Data Availability Statement

The data that support the findings of this study are available from the corresponding author upon reasonable request.

## Keywords

electrochemical transistors, in operando, organic mixed conductors, quartz crystal microbalance, swelling

Received: December 5, 2023
Revised: March 4, 2024
Published online: April 12, 2024

[1] S. Inal, J. Rivnay, A.-O. Suiu, G. G. Malliaras, I. McCulloch, *Acc. Chem. Res.* **2018**, *51*, 1368.
[2] J. Tropp, D. Meli, J. Rivnay, *Matter* **2023**, *6*, 3132.
[3] S. Inal, G. G. Malliaras, J. Rivnay, *Nat. Commun.* **2017**, *8*, 1767.
[4] P. Andersson Ersman, M. Zabihipour, D. Tu, R. Lassnig, J. Strandberg, J. Åhlin, M. Nilsson, D. Westerberg, G. Gustafsson, M. Berggren, R. Forchheimer, S. Fabiano, *Flexible Printed Electron.* **2020**, *5*, 024001.
[5] D. Majak, J. Fan, M. Gupta, *Sens. Actuators, B* **2019**, *286*, 111.

[6] K. Guo, S. Wustoni, A. Koklu, E. Díaz-Galicia, M. Moser, A. Hama, A. A. Alqahtani, A. Nazir Ahmad, F. Saeed Alhamlan, M. Shuaib, A. Pain, I. McCulloch, S. T. Arold, R. Grünberg, S. Inal, *Nat. Biomed. Eng.* **2021**, *5*, 666.
[7] X. Xi, D. Wu, W. Ji, S. Zhang, W. Tang, Y. Su, X. Guo, R. Liu, *Adv. Funct. Mater.* **2019**, *30*, 1905361.
[8] X. Tian, D. Liu, J. Bai, K. S. Chan, L. C. Ip, P. K. L. Chan, S. Zhang, *Anal. Chem.* **2022**, *94*, 6156.
[9] S.-K. Lee, Y. W. Cho, J.-S. Lee, Y.-R. Jung, S.-H. Oh, J.-Y. Sun, S. Kim, Y.-C. Joo, *Adv. Sci.* **2021**, *8*, 2001544.
[10] Y. Zhang, G. Ye, T. P. A. van der Pol, J. Dong, E. R. W. van Doremaele, I. Krauhausen, Y. Liu, P. Gkoupidenis, G. Portale, J. Song, R. C. Chiechi, Y. van de Burgt, *Adv. Funct. Mater.* **2022**, *32*, 2201593.
[11] J. Rivnay, S. Inal, B A. Collins, M. Sessolo, E. Stavrinidou, X. Strakosas, C. Tassone, D. M. Delongchamp, G. G. Malliaras, *Nat. Commun.* **2016**, *7*, 11287.
[12] S.-M. Kim, C.-H. Kim, Y. Kim, N. Kim, W.-J. Lee, E.-H. Lee, D. Kim, S. Park, K. Lee, J. Rivnay, M.-H. Yoon, *Nat. Commun.* **2018**, *9*, 3858.
[13] B. D. Paulsen, S. Fabiano, J. Rivnay, *Annu. Rev. Mater. Res.* **2021**, *51*, 73.
[14] H. Sun, J. Gerasimov, M. Berggren, S. Fabiano, *J. Mater. Chem. C* **2018**, *6*, 11778.
[15] H. Jia, T. Lei, *J. Mater. Chem. C* **2019**, *7*, 12809.
[16] S. Griggs, A. Marks, H. Bristow, I. McCulloch, *J. Mater. Chem. C* **2021**, *9*, 8099.
[17] Y. Wang, Y. Liu, *Trends Chem.* **2023**, *5*, P279.
[18] A. Giovannitti, C. B. Nielsen, D.-T. Sbircea, S. Inal, M. Donahue, M. R. Niazi, D. A. Hanifi, A. Amassian, G. G. Malliaras, J. Rivnay, I. McCulloch, *Nat. Commun.* **2016**, *7*, 13066.
[19] X. Liu, Y. Yan, Q. Zhang, K. Zhao, Y. Han, *Chem. Res. Chin. Univ.* **2021**, *37*, 1019.
[20] A. Giovannitti, I. P. Maria, D. Hanifi, M. J. Donahue, D. Bryant, K. J. Barth, B. E. Makdah, A. Savva, D. Moia, M. S. Zetek, P. R. F. Barnes, O. G. Reid, S. Inal, G. Rumbles, G. G. Malliaras, J. Nelson, J. Rivnay, I. McCulloch, *Chem. Mater.* **2018**, *30*, 2945.
[21] I. P. Maria, B. D. Paulsen, A. Savva, D. Ohayon, R. Wu, R. Hallani, A. Basu, W. Du, T. D. Anthopoulos, S. Inal, J. Rivnay, I. McCulloch, A. Giovannitti, *Adv. Funct. Mater.* **2021**, *31*, 2008718.
[22] I. P. Maria, S. Griggs, R. B. Rashid, B. D. Paulsen, J. Surgailis, K. Thorley, V. N. Le, G. T. Harrison, C. Combe, R. Hallani, A. Giovannitti, A. F. Paterson, S. Inal, J. Rivnay, I. McCulloch, *Chem. Mater.* **2022**, *34*, 8593.
[23] D. Jeong, I.-Y Jo, S. Lee, J. H. Kim, Y. Kim, D. Kim, J. R. Reynolds, M.-H. Yoon, B. J. Kim, *Adv. Funct. Mater.* **2022**, *32*, 2111950.
[24] X. Chen, A. Marks, B. D. Paulsen, R. Wu, R. B. Rashid, Hu Chen, M. Alsufyani, J. Rivnay, I. McCulloch, *Angew. Chem., Int. Ed.* **2021**, *60*, 9368.
[25] A. Marks, X. Chen, R. Wu, R. B. Rashid, W. Jin, B. D. Paulsen, M. Moser, X. Ji, S. Griggs, D. Meli, X. Wu, H. Bristow, J. Strzalka, N. Gasparini, G. Costantini, S. Fabiano, J. Rivnay, I. McCulloch, *J. Am. Chem. Soc.* **2022**, *144*, 4642.
[26] A. Savva, C. Cendra, A. Giugni, B. Torre, J. Surgailis, D. Ohayon, A. Giovannitti, I. McCulloch, E. Di Fabrizio, A. Salleo, J. Rivnay, S. Inal, *Chem. Mater.* **2019**, *31*, 927.
[27] A. A. Szumska, I. P. Maria, L. Q. Flagg, A. Savva, J. Surgailis, B. D. Paulsen, D. Moia, X. Chen, S. Griggs, J. T. Mefford, R. B. Rashid, A. Marks, S. Inal, D. S. Ginger, A. Giovannitti, J. Nelson, *J. Am. Chem. Soc.* **2021**, *143*, 14795.
[28] A. Savva, R. Hallani, C. Cendra, J. Surgailis, T. C. Hidalgo, S. Wustoni, R. Sheelamanthula, X. Chen, M. Kirkus, A. Giovannitti, A. Salleo, I. McCulloch, S. Inal, *Adv. Funct. Mater.* **2020**, *30*, 1907657.
[29] M. Moser, L. R. Savagian, A. Savva, M. Matta, J. F. Ponder, T. C. Hidalgo, D. Ohayon, R. Hallani, M. Reisjalali, A. Troisi, A. Wadsworth, J. R. Reynolds, S. Inal, I. McCulloch, *Chem. Mater.* **2020**, *32*, 6618.
[30] L. Q. Flagg, C. G. Bischak, J. W. Onorato, R. B. Rashid, C. K. Luscombe, D. S. Ginger, *J. Am. Chem. Soc.* **2019**, *141*, 4345.
[31] C. G. Bischak, L. Q. Flagg, K. Yan, T. Rehman, D. W. Davies, R. J. Quezada, J. W. Onorato, C. K. Luscombe, Y. Diao, C.-Z. Li, D. S. Ginger, *J. Am. Chem. Soc.* **2020**, *142*, 7434.
[32] L. Q. Flagg, J. W. Onorato, C. K. Luscombe, V. Bhat, C. Risko, B. Levy-Wendt, M. F. Toney, C. R. McNeill, G. Freychet, M. Zhernenkov, R. Li, L. J. Richter, *Chem. Mater.* **2023**, *35*, 3960.
[33] L. Tang, C. R. McNeill, *Macromolecules* **2022**, *55*, 7273.
[34] A. Luzio, L. Criante, V. D'Innocenzo, M. Caironi, *Sci. Rep.* **2013**, *3*, 3425.
[35] J. Surgailis, A. Savva, V. Druet, B. D. Paulsen, R. Wu, A. Hamidi-Sakr, D. Ohayon, G. Nikiforidis, X. Chen, I. McCulloch, J. Rivnay, S. Inal, *Adv. Funct. Mater.* **2021**, *31*, 2010165.
[36] S. Moro, N. Siemons, O. Drury, D. A. Warr, T. A. Moriarty, L. M. A. Perdigão, D. Pearce, M. Moser, R. K. Hallani, J. Parker, I. McCulloch, J. M. Frost, J. Nelson, G. Costantini, *ACS Nano* **2022**, *16*, 21303.
[37] A. Giovannitti, R. B. Rashid, Q. Thiburce, B. D. Paulsen, C. Cendra, K. Thorley, D. Moia, J. T. Mefford, D. Hanifi, D. Weiyuan, M. Moser, A. Salleo, J. Nelson, I. McCulloch, J. Rivnay, *Adv. Mater.* **2020**, *32*, 1908047.
[38] D. A. Warr, L. M. A. Perdigão, H. Pinfold, J. Blohm, D. Stringer, A. Leventis, H. Bronstein, A. Troisi, G. Costantini, *Sci. Adv.* **2018**, *4*, aas9543.
[39] J F. Ponder Jr, Hu Chen, A M. T. Luci, S. Moro, M. Turano, A L. Hobson, G S. Collier, L M. A. Perdigão, M. Moser, W. Zhang, G. Costantini, J R. Reynolds, I. McCulloch, *ACS Mater. Lett.* **2021**, *3*, 1503.
[40] R. K. Hallani, B. D. Paulsen, A. J. Petty, R. Sheelamanthula, M. Moser, K. J. Thorley, W. Sohn, R. B. Rashid, A. Savva, S. Moro, J. P. Parker, O. Drury, M. Alsufyani, M. Neophytou, J. Kosco, S. Inal, G. Costantini, J. Rivnay, I. McCulloch, *J. Am. Chem. Soc.* **2021**, *143*, 11007.
[41] J. Vanderspikken, Z. Liu, X. Wu, O. Beckers, S. Moro, T. J. Quill, Q. Liu, A. Goossens, A. Marks, K. Weaver, M. Hamid, B. Goderis, E. Nies, V. Lemaur, D. Beljonne, A. Salleo, L. Lutsen, K. Vandewal, B. Van Mele, G. Costantini, N. Van den Brande, W. Maes, *Adv. Funct. Mater.* **2023**, *33*, 2309403.
[42] S. Griggs, A. Marks, D. Meli, G. Rebetez, O. Bardagot, B. D. Paulsen, Hu Chen, K. Weaver, M. I. Nugraha, E. A. Schafer, J. Tropp, C. M. Aitchison, T. D. Anthopoulos, N. Banerji, J. Rivnay, I. McCulloch, *Nat. Commun.* **2022**, *13*, 7964.
[43] M. Brinkmann, E. Gonthier, S. Bogen, K. Tremel, S. Ludwigs, M. Hufnagel, M. Sommer, *ACS Nano* **2012**, *6*, 10319.
[44] V. Druet, D. Ohayon, C. E. Petoukhoff, Y. Zhong, N. Alshehri, A. Koklu, P. D. Nayak, L. Salvigni, L. Almulla, J. Surgailis, S. Griggs, I. McCulloch, F. Laquai, S. Inal, *Nat. Commun.* **2023**, *14*, 5481.
[45] L. Q. Flagg, L. E. Asselta, N. D'Antona, T. Nicolini, N. Stingelin, J. W. Onorato, C. K. Luscombe, R. Li, L. J. Richter, *ACS Appl. Mater. Interfaces* **2022**, *14*, 29052.
[46] L. Q. Flagg, R. Giridharagopal, J. Guo, D. S. Ginger, *Chem. Mater.* **2018**, *30*, 5380.
[47] M. Moser, T. C. Hidalgo, J. Surgailis, J. Gladisch, S. Ghosh, R. Sheelamanthula, Q. Thiburce, A. Giovannitti, A. Salleo, N. Gasparini, A. Wadsworth, I. Zozoulenko, M. Berggren, E. Stavrinidou, S. Inal, I. McCulloch, *Adv. Mater.* **2020**, *32*, 2002748.
[48] K. Feng, W. Shan, S. Ma, Z. Wu, J. Chen, H. Guo, B. Liu, J. Wang, B. Li, H. Y. Woo, S. Fabiano, W. Huang, X. Guo, *Angew. Chem., Int. Ed.* **2021**, *60*, 24198.
[49] Z. S. Parr, J. Borges-González, R. B. Rashid, K. J. Thorley, D. Meli, B. D. Paulsen, J. Strzalka, J. Rivnay, C. B. Nielsen, *Adv. Mater.* **2022**, *34*, 2107829.